Kinetic characterisation of a dye decolourising peroxidase from *Streptomyces lividans*: new insight into the mechanism of anthraquinone dye decolourisation

Amanda K. Chaplin, Michael T. Wilson, Jonathan A.R. Worrall[*]

School of Biological Sciences, University of Essex, Wivenhoe Park, Colchester, CO4 3SQ, U.K.

*To whom correspondence to be addressed: jworrall@essex.ac.uk; Tel: +44 (0)1206 872095

TABLE OF CONTENT GRAPHIC

A dye decolourising haem peroxidase from *Streptomyces lividans* decolourises the anthraquinone dye RB19 through a disproportionation mechanism.
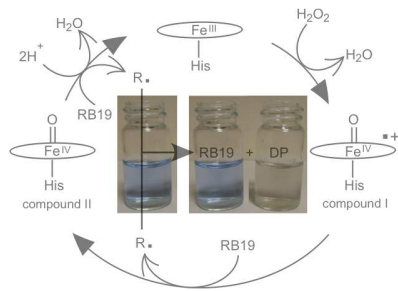
ABSTRACT

Dye decolourising peroxidases are the most recent family of haem peroxidases to be discovered. The oxidising potential of these enzymes is driven by the formation of ferryl intermediates that enables them to oxidise synthetic dye molecules that are widely used in the textile industry. We have investigated the catalytic cycle of a dye decolourising peroxidase (DtpA) from a biotechnologically important bacterium *Streptomyces lividans*. Using a combination of steady-state and stopped-flow kinetic investigations, we have determined the rate constants for all steps in the catalytic cycle with a range of substrate molecules. For most substrates, the value of k_{cat}/K_m measured by steady-state kinetics is equal to the slowest step in catalysis measured by stopped-flow spectroscopy, namely the decay of the ferryl $Fe^{IV}=O$ species (compound II) to form the ferric species. With the anthraquinone-based dye, reactive blue 19 (RB19) unusual steady-state kinetic behaviour is observed, which we propose through kinetic modelling of the catalytic cycle is due to a disproportionation mechanism of the dye. At low RB19 concentrations, the rate of disproportionation is slower than that of the rate determining step in DtpA, whereas at higher concentrations of RB19 the rate of disproportionation is faster. This mechanism obviates the need to postulate secondary sites for substrate binding on the enzyme which has been previously proposed for other dye decolourising haem peroxidases.

INTRODUCTION

Haem peroxidases undergo a two-electron oxidation and release of a H_2O molecule upon reaction with hydrogen peroxide (H_2O_2), followed by stepwise oxidation of an organic substrate, typically a phenol or aromatic amine [1]. In 1809, it was observed that the gum from the wood of guaiacum, a genus of flowering plant, turned blue in the mouth during its use as a dentifrice. Many years later a salivary peroxidase was discovered [2] and it was found that a phenol compound present in the guaiacum gum turned blue in the presence of a haem peroxidase and H_2O_2. Thus the 1809 observation may be considered as the first recorded peroxidase reaction. Over the past two centuries haem peroxidases have been extensively studied and phylogenetic analysis has revealed they are found throughout the three domains of life [3]. At the turn of the last century the most recent family of haem peroxidases, the so-called dye-decolorizing peroxidases (DyP), were discovered [4, 5]. As with nearly all haem peroxidases the physiological substrates of DyPs are unknown, but as their name suggests they possess the ability to oxidize dye molecules that include azo and anthraquinone-based dyes used in the textile industry [6]. Subsequent research has revealed that DyPs generally have a broad range of substrate specificity, which extends into the ability to oxidize manganese as well as lignin and lignocellulose into monocyclic phenol compounds [7-9]. Therefore, DyPs have vast potential for use in commercial biotechnology applications that may range from addressing textile waste to exploiting the release of reusable carbon from lignin [10].

DyPs have been classified into four sub-families (types A to D) based on amino-acid sequences [3]. Type A to C are widespread in bacteria, whereas type D are unique to fungi. The tertiary structure of DyPs are highly homologous between classes and comprise of two ferredoxin-like folds with the C-terminal domain housing a *b*-type haem [11] (Fig.1 A). The haem iron is coordinated in the proximal position by a His residue. At the distal side of the haem the H_2O_2 binds to the ferric iron. Following addition of H_2O_2, the initial steps of the catalytic cycle of DyPs are reported to be akin to other haem peroxidases [12]. A two-electron oxidation step to a high-valence iron intermediate occurs that generates a $Fe^{IV}=O$ group and a π-cation radical on the porphyrin ($[Fe^{IV}=O]^{\bullet+}$) referred to as compound I. Addition of a one-electron equivalent from a substrate molecule to compound I leads to the formation of compound II ($[Fe^{IV}=O]$), with the

donation of a second electron from a substrate molecule returning this intermediate to the ferric resting state [12]. On the distal haem side an Asp and Arg residue are positioned over the haem (Fig 1B). The Asp residue forms part of the *GXXDG* motif that is assigned as the fingerprint of all DyPs [11, 13]. In other haem peroxidase families, a distal His is found in the Asp position and serves to facilitate the shuttling of a proton from the Fe linked peroxide O atom to the distal peroxide O atom, thus promoting heterolytic fission of the O-O bond [14]. In DyPs the role of the distal Asp residue remains to be fully clarified. A current view is that its role may be dependent on the DyP sub-family.

Steady-state kinetic studies of DyPs with different substrates have dominated the kinetic literature on DyPs. Only one transient kinetic study providing rate constants for all the catalytic steps in the cycle has so far been reported [12]. Furthermore, a recent investigation with a fungal DyP (type D) has revealed unusual steady-state kinetics, whereby bimodal curves with various substrates including with anthraquinone-based dyes are observed [15]. These data have been interpreted to mean the existence of two catalytic surface sites for the substrate with different reactivities [15]. We have previously identified an A-type DyP in the bacterium *Streptomyces lividans*, which we named DtpA (dye-type decolorizing peroxidase A). In the present study, we have carried out a thorough kinetic analysis of the catalytic cycle of DtpA with a range of substrates (Fig. 1C). Herein we show that DtpA has a broad substrate specificity over a wide pH range compared to other DyPs. Interestingly, we also observe unusual steady-state kinetic behaviour with the anthraquinone-based dye molecule reactive blue 19 (RB19). Through careful transient and steady-state kinetic analysis together with subsequent kinetic modeling we reveal that the observed kinetics with RB19 are in fact a result of a dye disproportionation mechanism with no evidence for multiple substrate binding sites.

MATERIALS AND METHODS

Purification of DtpA, sample preparation and reagents used

Streptomyces lividans (*SLI4211*) DtpA was over-expressed in *Escherichia coli* and purified as previously reported [16]. Concentrations of purified DtpA were determined spectrophotometrically (Cary 60 UV-visible spectrophotometer (Agilent)) using an extinction coefficient (ε) at 280 nm of 37,470 M^{-1} cm^{-1} as determined using the ExPASy

server [17]. Stock DtpA samples were prepared in 20 mM sodium phosphate pH 7.0, 100 mM NaCl and diluted to a final concentration as required or exchanged into a desired buffer using a PD-10 column (Generon). Other buffers used were 10 mM sodium acetate pH 5.0, 100 mM NaCl and 20 mM boric acid pH 9.0 or 10.5, 100 mM NaCl. H_2O_2 solutions (Sigma-Aldrich) were prepared from a stock with the final concentration determined spectrophotometrically using an $\varepsilon = 43.6$ M^{-1} cm^{-1} at 240 nm [18]. Potassium ferricyanide ($K_3[Fe(CN)_6]$) (Sigma-Aldrich) concentrations were also determined using absorbance spectroscopy using an $\varepsilon = 1.04$ mM^{-1} cm^{-1} at 420 nm.

Steady-state kinetics

2,2-Azinobis(3-ethylbenthiazoline-6-sulfonic acid) (ABTS), veratryl alcohol (VA) 2,6-dimethyloxyphenol (2,6-DMP), guaiacol and reactive blue 19 (RB19) were all purchased from Sigma-Aldrich. Assays were set-up in 3 ml cuvettes and monitored using a Hewlett-Packard 8453 diode-array spectrophotometer scanning between 190 and 1100 nm and thermostatted at 25 ^{o}C. Each cuvette was baselined against DtpA (30-1000 nM) and a set concentration of a reducing substrate; ABTS (0.125-60 mM), VA (5-90 mM), 2,6-DMP (0.125-40 mM), $K_4[Fe(CN)_6]$ (0.125-80 mM), guaiacol (2.5-50 mM) and RB19 (10-150 μM) with the reaction then started by the addition of 0.2 mM H_2O_2. A turnover rate (v, s^{-1}) defined as the initial rate normalized to the DtpA concentration was calculated from $((\Delta A/\varepsilon/t)/[DtpA])$, where ΔA is the absorbance change at the specific substrate oxidation wavelength (ABTS = 436 nm, VA= 310 nm, 2,6-DMP = 469 nm, guaiacol = 470 nm, RB19 = 595 nm and $K_4[Fe(CN)_6]$ = 420 nm), ε is the extinction coefficient of the substrate oxidation product (ABTS = 29.3 mM^{-1} cm^{-1}, VA = 9.3 mM^{-1} cm^{-1}, 2,6-DMP = 27.3 mM^{-1} cm^{-1}, guaiacol = 5.57 mM^{-1} cm^{-1}, RB19 = 10 mM^{-1} cm^{-1} and $K_4[Fe(CN)_6]$ = 1.04 mM^{-1} cm^{-1}), t is the time in seconds and [DtpA] is the total concentration of DtpA (mM) in the assay. A non-linear least square fitting of the data using the Michaelis-Menten equation allowed for the parameters K_m and k_{cat} to be determined. The pH dependence of DtpA activity was carried out using a mixed buffer system comprising of 10 mM Tris, MES, MOPS, sodium acetate and 200 mM KCl with pH values between 4.0 and 9.5 used. For pH 10.0 and 10.5, 20 mM boric acid, 100 mM NaCl was used. The initial rates (Au/s) obtained were converted into percentage of relative activity with the

highest obtained activity taken as 100%.

Stopped-flow absorption kinetics

Transient kinetics of the interaction of H_2O_2 with ferric DtpA and reduction of compound I by a specific substrate were performed using a SX20 stopped-flow spectrophotometer (Applied Photophysics) equipped with a diode-array multi-wavelength unit or a single wavelength photomultiplier and thermostatted at 25 °C. Compound I formation was monitored at pH 7.0 using a solution of DtpA (5 μM after mixing), which was rapidly mixed with a series of H_2O_2 concentrations (12.5-75 μM after mixing). Time courses were taken at 406 nm and fitted to a single exponential function. The ProKineticist (Applied Photophysics) software was used to obtain pseudo-first order rate constants (k_{obs}). To monitor the reduction of compound I, DtpA (5 μM after mixing) was pre-loaded with one-equivalent of H_2O_2 and rapidly transferred to the stopped-flow working syringe, before rapidly mixing with an excess of ABTS (0.125-1 mM after mixing), $K_4[Fe(CN)_6]$ (25-150 μM after mixing) or RB19 (25-200 μM after mixing). Reactions with ABTS and RB19 were carried out at pH 5.0 and $K_4[Fe(CN)_6]$ was performed at pH 7.0. The overall spectral transitions were first monitored using the diode array unit, followed by monitoring at a single wavelength (420 nm) to observe the formation and decay of compound II. A double exponential function was required to fit the data and obtain k_{obs} values. All k_{obs} values obtained are an average of three replicates. To monitor steady-state kinetics of DtpA with RB19 using the stopped-flow spectrophotometer at pH 5.0 ferric DtpA (5 μM after mixing) was rapidly mixed with RB19 (10-150 μM) containing 100 μM H_2O_2 (after mixing) and values for *v* extracted as described (*vide supra*).

Kinetic modelling of RB19 oxidation

Simulation of the catalytic cycle of DtpA with RB19 under steady state conditions was performed in ProKineticist (Applied Photophysics) software using the model: a + b > c + d; c + b > e + d; e > a; 2d > f + b; where a = compound I DtpA, b = RB19 (RH), c = compound II DtpA, d = one-oxidizing equivalent of RB19 (R•), e = ferric DtpA, and f = decolorized RB19 product (DP). Rate constants for this simulation were k_1 = compound I

DtpA to compound II ($M^{-1}s^{-1}$), k_2 = DtpA compound II to ferric DtpA ($M^{-1}s^{-1}$), k_3 = ferric DtpA to compound I (s^{-1}) and k_4 = RB19 disproportionation ($M^{-1}s^{-1}$). Turnover rates for the simulations were determined as described above.

RESULTS AND DISCUSSION

Spectral characterisation and kinetics of DtpA compound I formation

The resting state ferric haem spectrum of DtpA is reported in Fig. 2. Addition of one-equivalent of H_2O_2 to the ferric state generates a new spectrum assigned as compound I ($[Fe^{IV}=O]^{\bullet+}$) with the subsequent one equivalent addition of the reductant $K_4[Fe(CN)_6]$ leading to a compound II spectrum ($[Fe^{IV}=O]$). These spectra are typical of high valent haem iron intermediate states generated in the catalytic cycle of a peroxidase. Corroboration of these state assignments was obtained through a series of titration experiments (Fig. 3). One equivalent of H_2O_2 is required to generate compound I (Fig. 3A), which in the absence of any reductant decays back to the ferric resting state without any detectable compound II species over a period of minutes ($t_{1/2} \sim 2.5$ min). This behaviour contrasts to peroxidases such as lignin peroxidase (LiP) and horse radish peroxidase (HRP) where compound I decays rapidly to compound II and then to ferric [19]. Therefore, for DtpA the observed behaviour indicates that the decay of compound II to ferric is faster than the decay of compound I to compound II.

Titration of up to one-equivalent of $K_4[Fe(CN)_6]$ to compound I generates compound II (Fig. 3B - black), with the addition of a second-equivalent of $K_4[Fe(CN)_6]$ giving the resting ferric state (Fig. 3B – green). Thus, DtpA acts in accord with other haem peroxidases in that it stores both oxidising equivalents of H_2O_2 within compound I. The kinetics of compound I formation were monitored by stopped-flow absorption spectroscopy (Fig. 3C). A linear dependence of pseudo first-order rate constants with increasing [H_2O_2] is observed (Fig. 3C), enabling a second-order rate constant, k = 8.9 ± 0.25 x 10^6 $M^{-1}s^{-1}$ at pH 7.0 to be determined. This second-order rate constant for DtpA is only marginally slower than the pH independent second-order rate constant for compound I formation in HRP (k = 1.8 x 10^7 $M^{-1}s^{-1}$) [20, 21] but faster than LiP (k = 6.5 x 10^5 $M^{-1}s^{-1}$) [19]. Two other A-type DyPs have had their compound I kinetics analysed. For *Thermomonospora curvata* DyP second-order rate constants of k = 5.9 x 10^6 $M^{-1}s^{-1}$ (pH

7.8) and 4.0 x 10^6 $M^{-1}s^{-1}$ (pH 3.0) have been determined [12] and from *Thermobifida fusca k* = 5.5 x 10^4 $M^{-1}s^{-1}$ (pH 5.5) [22]. Elsewhere, only two B-type DyPs have had their compound I kinetics determined with k = 1.8 x10^5 $M^{-1}s^{-1}$ (pH 7.5) for the DyP from *Rhodococcus jostii* [9] and k = 1.4 x 10^6 $M^{-1}s^{-1}$ (pH 7.0) for the DyP from *Pseudomonas putida* [23]. Thus, a significant variation in compound I formation within the DyP family and within sub-families is apparent, with the absence of data on types C and D notable exceptions, highlighting the need for further kinetic studies to build a complete picture of the catalytic properties of this class of haem peroxidase.

Steady-state peroxidase activity reveals a variation in catalytic efficiency between substrates

Activity assays of DtpA using a series of reducing substrates (Fig. 1C) were carried out under steady-state conditions. Previous studies with DyPs have highlighted an activity optimum between pH 3.0 and 4.0. For DtpA the optical properties of the Soret region were significantly perturbed below pH 4.0, which we attribute to a denaturation of the enzyme and loss of haem. Initial activity assays with the various substrates were carried out over a pH range between 4.0 and 10.5, where clear pH activity optima were observed for the different substrates. Extensive steady-state assays were carried out at the pH optima for the respective substrate, and at a second pH where activity was determined to be lower. In contrast with the other substrates tested, VA showed activity only at pH 5.0. The calculated steady-state parameters, k_{cat} and K_m for the various substrates are reported in Table 1, with illustrative Michaelis-Menten plots shown in Fig. 4. We note that the activity with 2,6-DMP and VA, the latter a preferred substrate for LiP [24, 25], despite being low, contrasts with the A-type DyP from *T. curvata* [12] where no activity with 2,6-DMP and VA was observed. From Table 1 it is apparent that DtpA is the most catalytically efficient with $K_4[Fe(CN)_6]$ and ABTS at pH 5.0 based on the k_{cat}/K_m values. For the phenolic substrates, 2,6-DMP and guaiacol, higher activity is observed at more alkaline conditions (Fig, 4B and Table 1). This could be due to these substrates having a protonatable hydroxyl group (pK_a between 9.0 and 11.0) suggesting that to act as electron donors to DtpA, they must be deprotonated. In contrast $K_4[Fe(CN)_6]$, ABTS and VA do not have protonatable groups and therefore the maximum activity observed is dependent

on DtpA rather than a physicochemical property of the substrate. Furthermore, this acidic pH dependency is also consistent with the chemistry of ferryl iron ($Fe^{IV}=O$), which is a better oxidant at lower pH values.

The rate limiting step in the DtpA catalytic cycle is between compound II and the ferric species

To elucidate the individual steps of the steady-state mechanism for DtpA, we undertook a series of pre-steady state kinetic measurements using stopped-flow spectroscopy with the most active substrates; ABTS and $K_4[Fe(CN)_6]$. In these experiments, each time course represents the reaction of a separate sample of compound I made *de novo* (*i.e.* all measurements made before spontaneous decay of compound I). On mixing compound I with $K_4[Fe(CN)_6]$ at pH 5.0 rapid reactions could be discerned, but too rapid to determine rate constants with confidence. At pH 7.0, however, reasonable reaction rates were observed allowing data to be collected. Each time course collected at 420 nm comprised a rapid increase in absorbance followed by a slower bleaching (Fig. 5). Global analysis of the full spectral data (Fig. 5A and inset) showed that these phases could be assigned as the fast reaction of compound I to compound II and the slower reaction of compound II to the ferric resting state. Pseudo-first order rate constants for each phase of the time course were found to be $K_4[Fe(CN)_6]$ concentration dependent (Fig. 5B and C) and these linear dependences allowed the second order rate constants for each step (k_1 and k_2) to be determined and reported in Table 1. Similar behaviour was observed for ABTS at pH 5.0 (data not shown). Spectral analysis led to the same assignment of the phases with k_1 and k_2 values determined and reported in Table 1. Importantly, the k_2 values observed are comparable under the same conditions to the k_{cat}/K_m values determined under steady-state conditions corroborating the view that the slow step assigned to transition from compound II to ferric resting state is the rate limiting step in DtpA.

Steady-state kinetics of DtpA with RB19 yield non-hyperbolic Michaelis-Menten plots

The kinetics of the decolourisation of the anthraquinone dye RB19 was also investigated. As these peroxidases have potential in bioremediation to detoxify textile waste, understanding the details of the reaction kinetics is important for future applications. In

contrast to the substrates described above, RB19 behaves very differently. Figure 6A shows the results from the steady-state kinetics of RB19 decolourisation by DtpA through monitoring the absorbance decrease of the dye at 595 nm at pH values of 4.0 and 5.0. It is clear from the turnover rates (v, s^{-1}) that DtpA is more active at pH 4.0 and no activity was observed under steady-state conditions at pH 7.0. However, the plots of v, s^{-1} as a function of RB19 concentration at pH 4.0 and 5.0 do not conform to simple hyperbolae (Fig. 6A) and thus an alternative approach to described the kinetics is required (*vide infra*). Furthermore, the data are not bimodal (*i.e.* comprising two hyperbolae) as reported for the fungal DyP from *Auricularia auricular-judae* [15]. Rather, the initial portion of each plot displays little activity until a threshold concentration of RB19 is reached, which differs depending on pH (Fig. 6A). This unusual behaviour was further explored by undertaking stopped-flow experiments at pH 5.0, using higher DtpA and H_2O_2 concentrations. In these experiments, DtpA entered steady-state and thereafter the dye decolourised, with turnover rates following a similar trend to those obtained using conventional spectroscopy (Fig. 6A).

RB19 is decolourised through a disproportionation mechanism

As outlined above for $K_4[Fe(CN)_6]$ and ABTS, two kinetic phases were again observed on reacting compound I with RB19 at pH 5.0. Global analysis of the full spectral data showed that these phases could again be assigned as the fast reaction of compound I to form compound II and the slower reaction of compound II to form the ferric resting state. It is noteworthy that both one-electron reduction steps, compound I to II and compound II to ferric, are dependent on the bulk RB19 concentration and are thus second-order (Fig. 6B), with k_1 and k_2 values reported in Table 1. This means that although the reaction of RB19 requires two-electrons for complete oxidation, this is *not* achieved in one step by DtpA. If it were otherwise, then the rate constant of the first step would be dependent on bulk RB19 concentration, while the second step would be independent. Furthermore, by exploring the time range just sufficient to take compound I to compound II (~1 s) at pH 5.0, we observe that DtpA undergoes a spectral transition but the dye is not bleached. This latter conclusion is indicated by the difference spectrum in Fig. 6C. This shows that while the dye is donating a single electron to DtpA, effecting the spectral transition

compound I to compound II, the dye does not decolourise at pH 5.0 (Fig. 6C). In contrast at pH 7.0, where it is possible to observe only the transformation of compound I to compound II there is a simultaneous bleaching in the 595 nm region (Fig. 6C).

Taking into consideration this observation at pH 7.0, the two concentration dependent steps and the absence of the bleaching of the 595 nm absorption band at pH 5.0, leads us to suggest that the dye decolourises through a disproportionation mechanism that involves single oxidised products (R•). In this way two single-electron-oxidised RB19 molecules (R• + R•) interact to form one RB19 molecule (RH) and one RB19 (DP) with both oxidising equivalents (Fig. 7A). Formation of the latter (DP) results in decolourisation of the dye. This proposal affords an explanation for the non-Michaelis-Menten behaviour at pH 5.0 (Fig. 6A). At low RB19 concentrations, the rate of disproportionation is slower than that of the rate determining step in DtpA, because the concentration of R• is low. At higher concentrations of RB19 the rate of disproportionation becomes faster as R• concentration becomes higher (Fig. 6A). This conclusion is reasonable as disproportionation is a second-order process and will increase in rate as the concentration of the dye increases, whereas the rate-limiting step in DtpA is first-order and will be unaffected by dye concentration. Thus, we propose that at pH 7.0 the disproportionation rate must be faster than the internal rate of DtpA, compared to at pH 5.0.

Simulation of the steady-state RB19 assay

To gain further insight into our proposal that RB19 undergoes bleaching through disproportionation we have modelled the steady-state based on the catalytic cycle for DtpA depicted in Figure 7A. The model postulated can however only simulate the initial portion of the non-Michaelis-Menten curve as it does not contain steps involving saturable substrate sites and thus V_{max} values will not be reached. Rate constants for the simulation have been chosen by reference to our transient stopped-flow experiments with either H_2O_2 or RB19 (Table 1, and Fig. 3C). We have however, needed to select a value of k_2 somewhat higher than found in transient kinetics (*i.e.* 600 $M^{-1}s^{-1}$ rather than 200 $M^{-1}s^{-1}$). This higher value was obtained from the slope of the linear portion of the steady-state plot (following the initial plateau region, Fig. 6A) as this slope should give, when

normalized to DtpA concentration, the rate constant of the rate limiting step, namely k_2. We have conducted simulations using a range of values for k_4 (rate constant for disproportionation). We illustrate in Fig. 7B simulations with a lower value (k_4 = 500 M^{-1}s^{-1}) which becomes the rate-limiting step in decolourisation and a higher value (k_4 = 70,000 M^{-1}s^{-1}) which maintains the rate limit within DtpA (k_2). Plots of these simulations compared to the experimentally determined turnover numbers obtained using stopped-flow spectroscopy are reported in Fig. 7B. Using a low disproportionation rate (k_4 = 500 M^{-1}s^{-1}) we observe a plot that mirrors the experimental data (pH 5.0) (*i.e.* little decolourisation until an apparent threshold of RB19 concentration is reached). At a higher disproportionation rate (k_4 = 70,000 M^{-1}s^{-1}) the simulation displays no initial 'lag-phase'. The turnover number now is linearly dependent on RB19 concentration, with the slope as expected being k_2, *i.e.* the rate-limiting step in the reaction under these conditions.

Finally, by analogy of the decolourisation of the anthraquinone dye, reactive blue 5 (RB5) [6, 26], we propose that the decolourisation of RB19 occurs through the cleavage of the secondary amine bond to yield an initial imine anthraquinonoid, which through hydrolysis can lead to further products, and a sulfatoethylsulfonylaniline (Fig 7C). Cleavage and thus decolourisation only occurs after removal of a second electron by DtpA, with subtraction of a single electron leaving conjugation intact and decolourisation does not occur (*vide supra*).

CONCLUSIONS

The DyP family is the most recent family of haem peroxidases to be identified. Whilst it is known that their catalytic cycle goes via high-valent haem iron intermediates, as confirmed in the present work, there is a distinct lack of kinetic data available across the four DyP sub-families for the individual steps in the catalytic cycle (Fig. 7A). In the present study using stopped-flow absorption spectroscopy, we have fully characterised the kinetics of each of the steps in the catalytic cycle of DtpA with various substrates, and have also modelled the disproportionation rate of the dye molecule RB19 (Fig. 7B). This analysis now paves the way for future work using site-directed variants of DtpA to interrogate the contribution of the distal Asp and Arg residues (Fig. 1B) in facilitating

formation of compound I and in the formation of the ferric resting state from compound II.

For DtpA we find that compound I formation is very rapid having a second-order rate constant only marginally slower than that reported for HRP [20, 21]. Other DyPs, including members of the A and B types, have notably slower rates of compound I formation [9, 22]. This reinforces a current view that the contribution of the distal Asp and Arg residues in facilitating compound I formation following binding of H_2O_2 varies amongst DyPs. To address this, systematic investigations are required with a member of each DyP sub-family that will encompass transient kinetic studies, site-directed variants and careful structural investigations using advancing technologies such as serial femtosecond crystallography coupled to *in crystallo* spectroscopies [27-29].

Under ambient conditions DtpA forms a relatively long-lived compound I state ($t_{1/2}$ = 2.5 min) allowing for the kinetics of the remaining steps in the catalytic cycle (Fig. 7A) to be determined. Notably, the rate limiting step for DtpA is k_2 or k_{cat}/K_m (Table 1) and not the formation of compound I which is significantly more rapid. However, the A-type DyP from *T. curvata* displays a k_{cat}/K_m of 1.7 x 10^7 $M^{-1}s^{-1}$ for ABTS, compared to 1.55 x 10^3 $M^{-1}s^{-1}$ for DtpA, and has a second-order rate constant for compound I formation of 10^6 $M^{-1}s^{-1}$ [12]. Thus, for *T. curvata* DyP reacting with ABTS the formation of compound I is now rate-limiting. This serves to illustrate that even within the same sub-family of DyPs there are variations in the step which is rate limiting in the catalytic cycle. Such differences have been suggested to arise because of the reducing substrate binding to specific surface sites rather than gaining access to the haem pocket. Oxidation then occurs through a long-range electron transfer mechanism from the surface site to the haem. Such a mechanism can account for how DyPs oxidize bulky dye molecules and lignin polymers. Therefore, DyPs will have likely evolved surface binding sites that suit certain types of substrates better than others and result in reactivity differences amongst species. Of note from this study is the finding that DtpA is active with 2,6-DMP and VA in comparison with other A-type DyPs. This therefore is an example of variation within DyP sub-familes for substrate activity. Furthermore, the fact that VA can be oxidised by this bacterial DyP has implications for use in microbial engineering approaches tailored towards lignin degradation.

The fact we account for the initial plateau region in the steady-state assays (Fig. 6A) with DtpA reacting with RB19 allows us to suggest that where such plateaus have been reported previously and explained by multiple low-activity binding sites may need revision [15]. The hypothesis that the plateau is due to slow disproportionation being rate limiting at low concentrations of dye and ceasing to be rate-limiting at high concentrations fits the kinetic analysis and the chemistry of the anthraquinone dyes. Moreover, this hypothesis is simple and requires no postulation of further substrate binding sites for which little evidence can be gained from structural and kinetic analysis of these enzyme.

ACKNOWLEDGEMENTS

REFERENCES

1. H. B. Dunford, *Peroxidases and Catalases: Biochemistry, Biophysics, Biotechnology, and Physiology*, Wiley, 2nd edn., 2010.
2. M. Morrison, P. Z. Allen, J. Bright and W. Jayasinghe, *Arch Biochem Biophys*, 1965, **111**, 126-133.
3. N. Fawal, Q. Li, B. Savelli, M. Brette, G. Passaia, M. Fabre, C. Mathe and C. Dunand, *Nucleic Acids Res*, 2013, **41**, D441-444.
4. S. J. Kim and M. Shoda, *Appl Environ Microbiol*, 1999, **65**, 1029-1035.
5. Y. Sugano, K. Sasaki and M. Shoda, *J Biosci Bioeng*, 1999, **87**, 411-417.
6. Y. Sugano, Y. Matsushima, K. Tsuchiya, H. Aoki, M. Hirai and M. Shoda, *Biodegradation*, 2009, **20**, 433-440.
7. M. Ahmad, C. R. Taylor, D. Pink, K. Burton, D. Eastwood, G. D. Bending and T. D. Bugg, *Mole Biosyst*, 2010, **6**, 815-821.
8. M. Ahmad, J. N. Roberts, E. M. Hardiman, R. Singh, L. D. Eltis and T. D. Bugg, *Biochemistry*, 2011, **50**, 5096-5107.
9. J. N. Roberts, R. Singh, J. C. Grigg, M. E. Murphy, T. D. Bugg and L. D. Eltis, *Biochemistry*, 2011, **50**, 5108-5119.
10. T. D. Bugg, M. Ahmad, E. M. Hardiman and R. Singh, *Curr Opin Biotech*, 2011, **22**, 394-400.
11. Y. Sugano, R. Muramatsu, A. Ichiyanagi, T. Sato and M. Shoda, *J Biol Chem*, 2007, **282**, 36652-36658.
12. C. Chen, R. Shrestha, K. Jia, P. F. Gao, B. V. Geisbrecht, S. H. Bossmann, J. Shi and P. Li, *J Biol Chem*, 2015, **290**, 23447-23463.
13. Y. Sugano, *Cell Mol Life Sci* 2009, **66**, 1387-1403.
14. T. L. Poulos and J. Kraut, *Journal Biol Chem*, 1980, **255**, 8199-8205.

15. D. Linde, R. Pogni, M. Canellas, F. Lucas, V. Guallar, M. C. Baratto, A. Sinicropi, V. Saez-Jimenez, C. Coscolin, A. Romero, F. J. Medrano, F. J. Ruiz-Duenas and A. T. Martinez, *Biochem. J*, 2015, **466**, 253-262.
16. M. L. Petrus, E. Vijgenboom, A. K. Chaplin, J. A. Worrall, G. P. van Wezel and D. Claessen, *Open Biol*, 2016, **6**.
17. E. Gasteiger, A. Gattiker, C. Hoogland, I. Ivanyi, R. D. Appel and A. Bairoch, *Nucleic Acids Res*, 2003, **31**, 3784-3788.
18. R. F. Beers, Jr. and I. W. Sizer, *J Biol Chem*, 1952, **195**, 133-140.
19. L. Marquez, H. Wariishi, H. B. Dunford and M. H. Gold, *J Biol Chem*, 1988, **263**, 10549-10552.
20. J. F. Holzwarth, F. Meyer, M. Pickard and H. B. Dunford, *Biochemistry*, 1988, **27**, 6628-6633.
21. J. N. Rodriguez-Lopez, A. T. Smith and R. N. Thorneley, *J Biol Chem*, 1996, **271**, 4023-4030.
22. R. Rahmanpour, D. Rea, S. Jamshidi, V. Fulop and T. D. Bugg, *Arch Biochem Biophys*, 2016, **594**, 54-60.
23. S. Mendes, V. Brissos, A. Gabriel, T. Catarino, D. L. Turner, S. Todorovic and L. O. Martins, *Arch Biochem Biophys*, 2015, **574**, 99-107.
24. K. Valli, H. Wariishi, M. H. Gold, D. C. Goodwin, S. D. Aust and T. A. Grover, *Biochemistry*, 1990, **29**, 8535-8539.
25. D. C. Goodwin, S. D. Aust and T. A. Grover, *Biochemistry*, 1995, **34**, 5060-5065.
26. D. Linde, F. J. Ruiz-Duenas, E. Fernandez-Fueyo, V. Guallar, K. E. Hammel, R. Pogni and A. T. Martinez, *Arch Biochem Biophys*, 2015, **574**, 66-74.
27. I. Schlichting, *IUCrJ*, 2015, **2**, 246-255.
28. J. M. Martin-Garcia, C. E. Conrad, J. Coe, S. Roy-Chowdhury and P. Fromme, *Arch Biochem Biophys*, 2016, **602**, 32-47.
29. D. Kekilli, T. Moreno-Chicano, A. K. Chaplin, S. Horrell, F. S. N. Dworkowski, J. A. R. Worrall, R. W. Strange and M. A. Hough, *IUCrJ*, 2017, **4,** 263-270.

Table 1: Steady-state kinetic parameters and second-order rate constants obtained from stopped-flow measurements for *S. lividans* DtpA with the various substrates at 25 $^{\circ}$C. Values in parenthesis are standard errors.

Steady-state kinetics				
Substrate	pH	K_m (mM)	k_{cat} (s^{-1})	k_{cat}/K_m (M^{-1}s^{-1})
ABTS	5.0	0.73 (0.2)	1.12 (0.15)	[a]1.53 x 10^3
	7.0	10.4 (0.8)	0.50 (0.05)	48
K$_4$[Fe(CN)$_6$]	5.0	3.1 (0.6)	295 (9)	9.5 x 10^4
	7.0	16.3 (1.8)	109 (4)	[b]6.7 x 10^3
VA	5.0	16.0 (1.2)	0.82 (0.03)	51
2,6-DMP	7.0	15.3 (1.6)	0.10 (0.02)	6.5
	9.0	5.6 (0.1)	0.32 (0.02)	57
Guaiacol	7.0	17.5 (0.3)	0.054 (0.005)	3.1
	10.5	28.1 (4.9)	0.40 (0.06)	14.2
Stopped-flow kinetics				
Substrate	pH	k_1 (M^{-1}s^{-1})	k_2 (M^{-1}s^{-1})	
ABTS	5.0	8.8 (0.4) x 10^3	[a]1.0 (0.1) x 10^3	
K$_4$[Fe(CN)$_6$]	7.0	1.3 (0.1) x 10^6	[b]7.1 (0.2) x 10^3	
RB19	5.0	7.4 (0.4) x 10^4	2.0 (0.1) x 10^2	

[a, b]Rate determining step (k_2) comparable to the steady-state k_{cat}/K_m rate
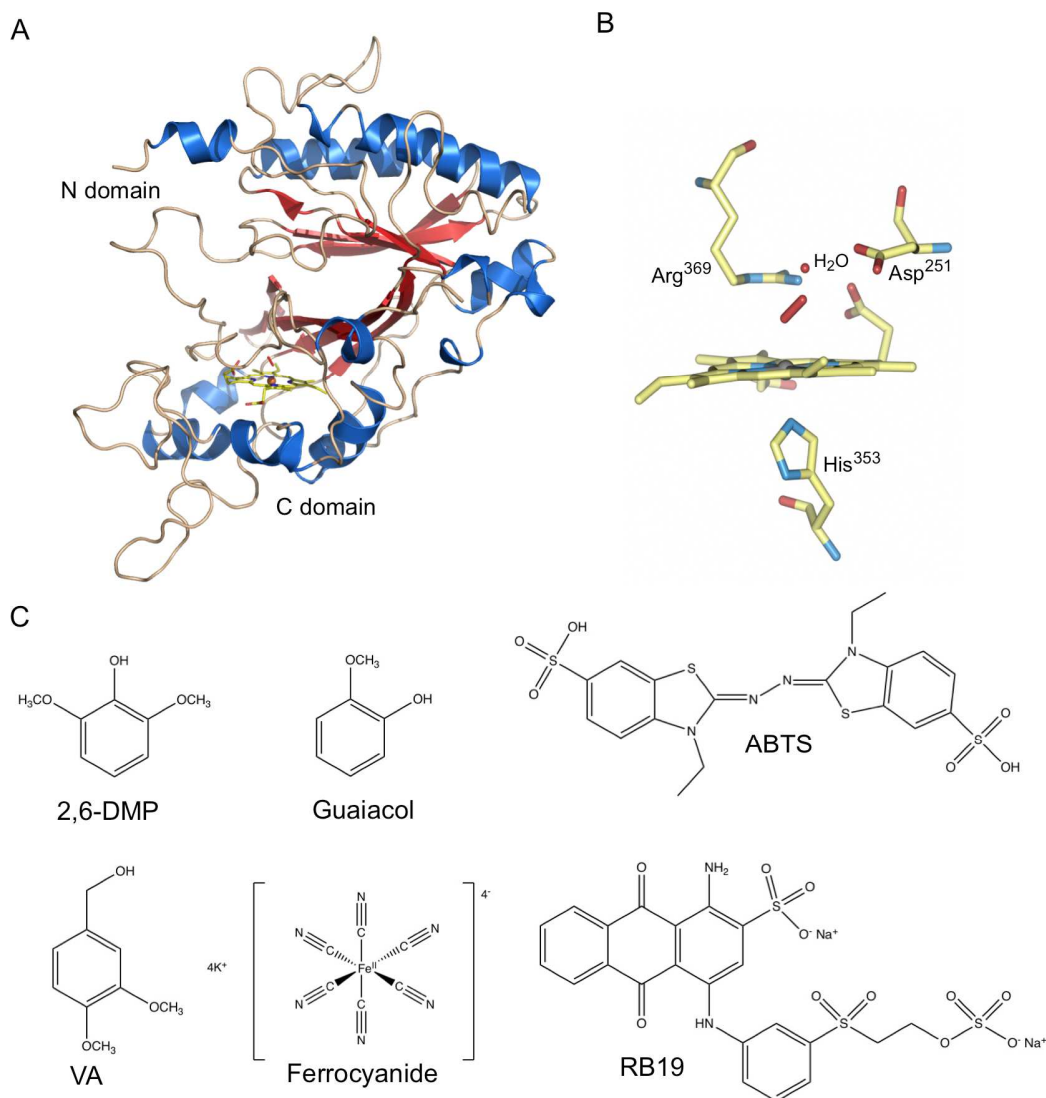
Figure 1: Structure of DtpA and substrates used in this study. A) Cartoon representation of the X-ray crystal structure of an A-type dye decolorizing peroxidase (DtpA) from *Streptomyces lividans* (PDB identifier 5mjh) [29]. The structure was determined in the oxy-ferrous form and spectroscopically validated through *in crystallo* spectroscopy [29]. The location of the *b*-type haem is shown in stick representation (yellow) in the C domain. B) The haem and proximal His residue and two key distal amino-acid residues in the oxy-ferrous DtpA structure. The bound distal dioxygen is indicated as a red stick. C) The chemical structures of the substrates used in the kinetic studies with DtpA.
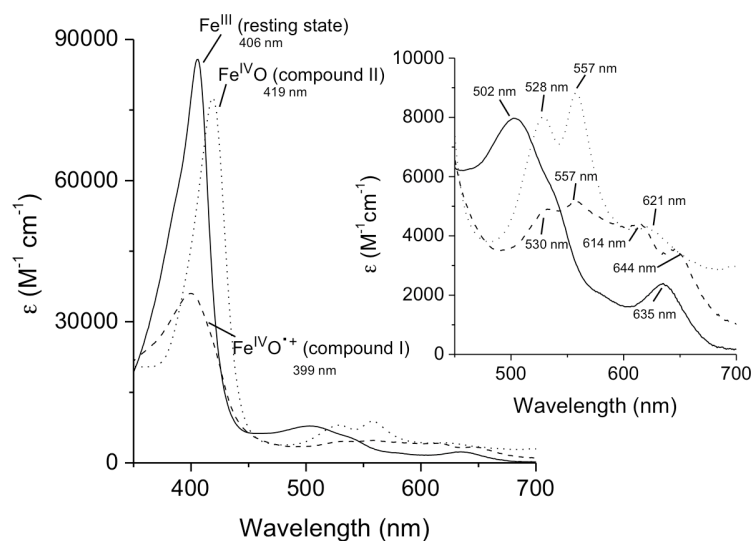
Figure 2: UV-visible absorbance spectra of DtpA at pH 7.0. The different haem oxidation states of DtpA (8 μM) are indicated along with the wavelength of the absorbance maxima of the Soret band. Compound I was formed following addition of one-equivalent H_2O_2 to the resting ferric state enzyme with compound II formed from compound I by addition of one equivalent $K_4(Fe(CN)_6)$. Inset shows a close-up of the Q-bands with wavelengths indicated.
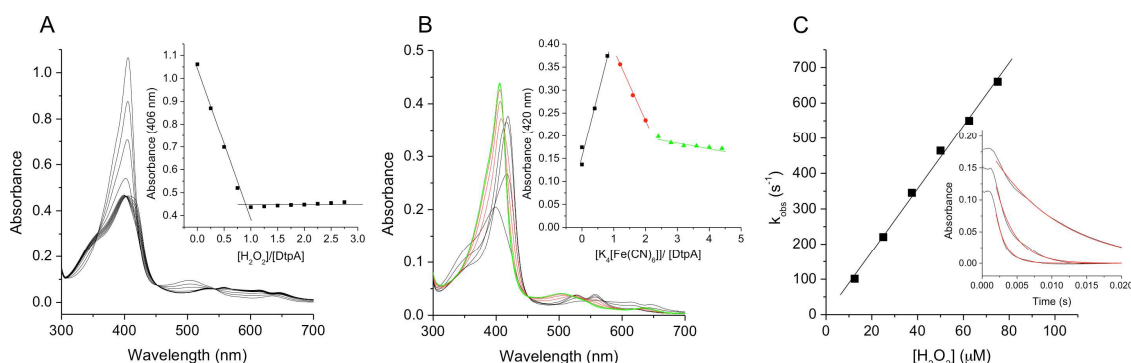
Figure 3: Formation of haem catalytic intermediates in DtpA at pH 7.0. A) Changes in the ferric absorbance spectrum upon titrating H_2O_2 to generate compound I. Absorbance changes (inset) at 406 nm plotted as a function of $[H_2O_2]/[DtpA]$, indicating a stoichiometry of one H_2O_2. B) Changes in the compound I absorbance spectrum upon titration with $K_4[Fe(CN)_6]$. Absorbance changes (inset) monitored at 420 nm plotted as a function of $[K_4[Fe(CN)_6]]/[DtpA]$. Compound II is formed following one equivalent of $K_4[Fe(CN)_6]$ (black), and the ferric resting state after the second equivalent (red), with no further spectral change on subsequent additions (green). C) A plot of pseudo first-order rate constants against $[H_2O_2]$ obtained from monitoring the formation of compound I using stopped-flow absorption spectroscopy at 406 nm. The data points are fitted to a linear function to obtain a second-order rate constant. Inset, example time traces (at 12.5, 37.5 and 75 μM H_2O_2) fitted (after the flow period of ~ 2 ms) to a single exponential function (red line).
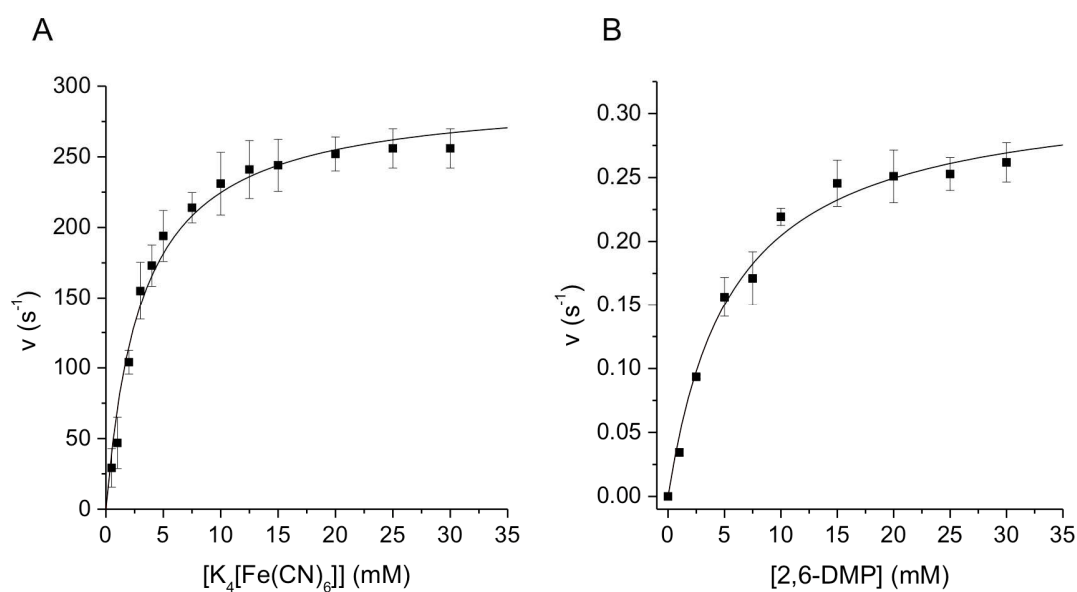
Figure 4: Steady-state kinetics of DtpA. Illustrative examples of turnover rates (v, s^{-1}) as defined in Materials and Methods for A) DtpA with $K_4[Fe(CN)_6]$ at pH 5.0 (k_{cat} = 295 ± 9 s^{-1} K_m = 3.1 ± 0.6 mM) and B) DtpA with 2,6-DMP at pH 9.0 (k_{cat} = 0.32 ± 0.02 s^{-1} K_m = 5.6 ± 0.1 mM). The solid line through the data points represents a fit to the Michaelis-Menten equation.
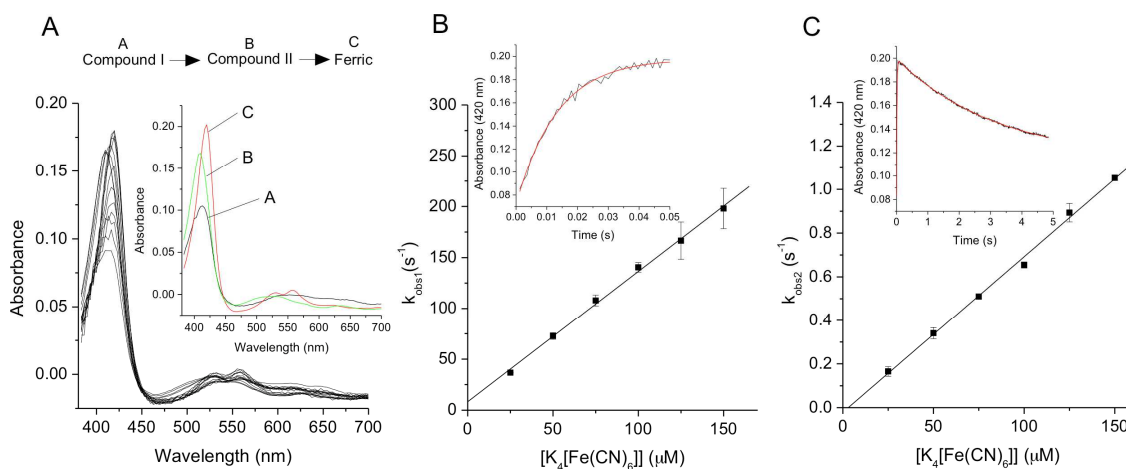
Figure 5: Stopped-flow kinetic analysis of DtpA compound I reduction by $K_4[Fe(CN)_6]$ at pH 7.0. A) UV-visible spectral changes upon mixing $K_4[Fe(CN)_6]$ (125 μM after mixing) with *de novo* prepared compound I DtpA (5 μM after mixing). Inset, global fitting using a sequential mechanism of a > b > c with A, B and C identified as compound I, compound II and resting state ferric, respectively. B and C) Observed pseudo first-order rate constants (k_{obs1} and k_{obs2}) plotted against increasing $K_4[Fe(CN)_6]$ concentrations for the fast phase (k_{obs1}) and slow phase (k_{obs2}) measured at 420 nm. Data points were fitted to a linear function to yield second-order rate constants reported in Table 2. Insets, example time courses for the fast (B) and slow (C) phases with the red line the exponential fit to the transient data.
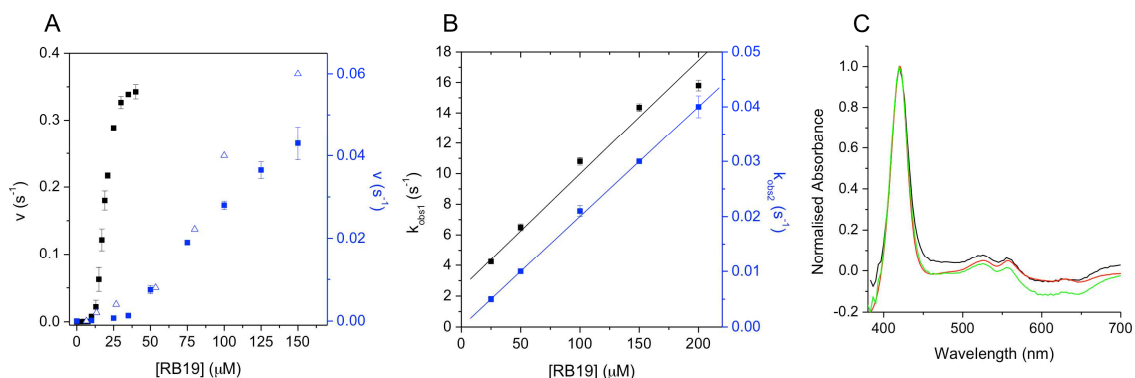
Figure 6: RB19 kinetics. A) Steady-state kinetics of DtpA with RB19 at pH 4.0 (black squares) and pH 5.0 (blue squares). Steady-state data were obtained using stopped-flow (as described in Materials and Methods) at pH 5.0 plotted as open blue triangles. B) Pseudo-first order rate constants (k_{obs1} and k_{obs2}) obtained from transient stopped-flow kinetics of compound I reduction as a function of RB19 concentration at pH 5.0. C) Difference spectra between compound I and compound II obtained after mixing in the stopped-flow with RB19 at pH 5.0 (black) and pH 7.0 (green) and the difference spectrum between compound I and compound II after titrating compound I DtpA with $K_4[Fe(CN)_6]$ (red).
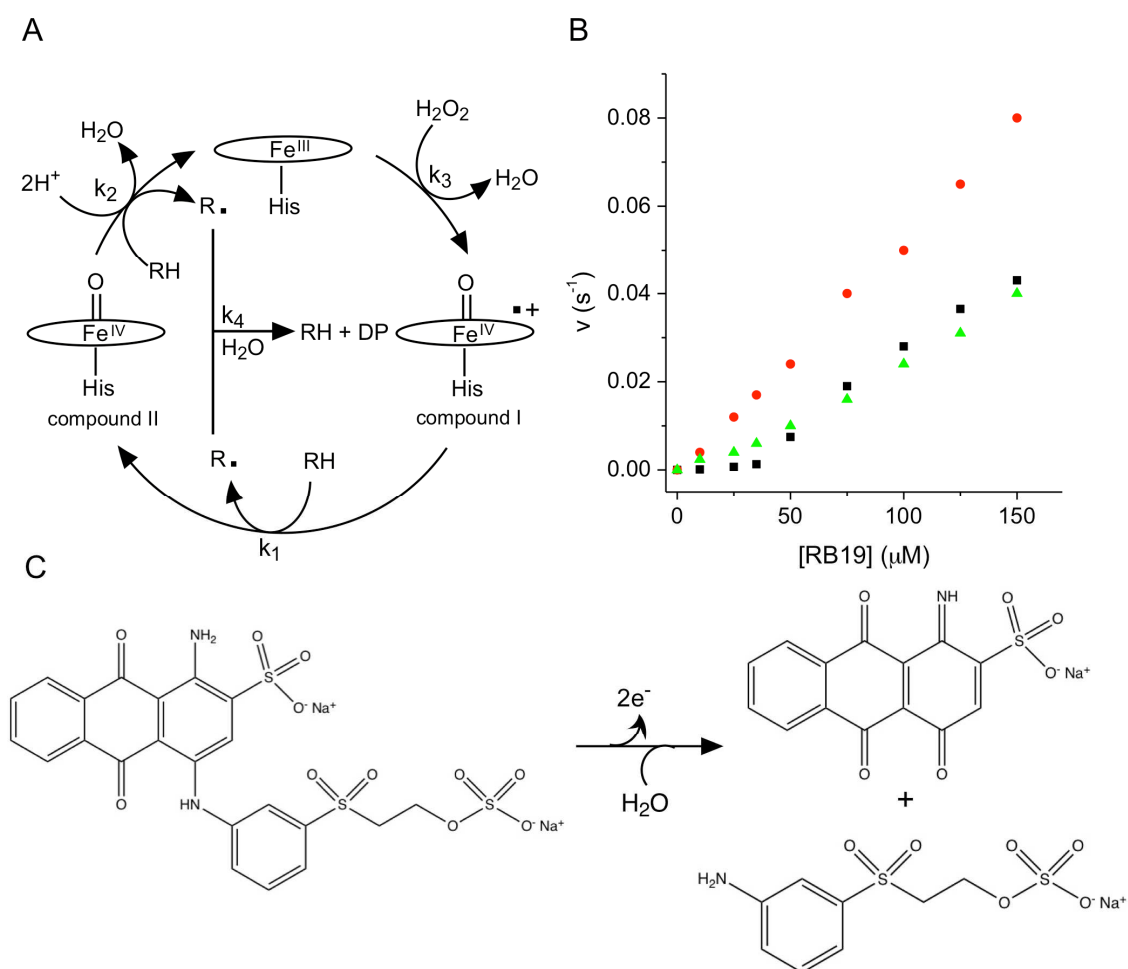
Figure 7: Modelling RB19 steady-state kinetics and dye decolourisation. A) Catalytic cycle for DtpA in the presence of H_2O_2 and RB19. The rate constants k_1, k_2 and k_3 have been determined experimentally as described in the main text and presented in Table 1, with k_4 the disproportionation rate constant obtained through simulation. B) Comparison of simulated and experimental values of v (the initial rate normalized to the enzyme concentration). Black squares represent the experimental data derived from the stopped-flow steady-state experiment taken from Figure 6A (open blue triangles). The simulations were performed with k_1 = 7.4 x 10^4 $M^{-1}s^{-1}$, k_2 = 600 $M^{-1}s^{-1}$ and k_3 = 1 x 10^4 s^{-1} (equivalent to a constant concentration of ~ 100 µM H_2O_2). The red circles represent a simulation in which k_4 is high k_4 = 70,000 $M^{-1}s^{-1}$ and the green triangles represent a simulation in which k_4 is low k_4 = 500 $M^{-1}s^{-1}$. C) The proposed chemistry of RB19 oxidation by DtpA

to yield two initial products.